9
Synthesis, Structure and Hirshfeld Surface Analyses of Diorganostannoxanes Assembled Using Intramolecular Coordination Approach

Research Article based on this study:

Mishra, A., Betal, A., Kamboj, N., Lama, P., Ji, R. S., Sahu, S., and Metre, R. K., (2022), "Diorganostannoxanes Stabilized by Intramolecular N→Sn Coordination Approach: Synthesis, Structure, TD-DFT and Hirshfeld Surface Analysis", *Journal of Molecular Structure*, Vol.1255, p.132478.

9.1 Introduction

Advances in coordination chemistry resulted in the fascinating applications of molecular organometallic complexes. More recently, molecular organometallic complexes have attracted the interest of the scientific community with their applications in various fields like organic light-emitting diodes (OLEDs) [Petrenko et al., 2020; Zhuang et al., 2019], organic field emitting transistors (OFETs) [Lu et al., 2019], resistive molecular memories [Mishra et al., 2020; Niklas et al., 2019], etc. Under the category of organometallic complexes, organostannoxanes are known for their diverse structures, which can be obtained as the result of a subtle change in the reaction conditions. Furthermore, the biological properties of such organotin compounds are well documented in the literature [Banti et al., 2019; Devi et al., 2018; Hu et al., 2018; Wang et al., 2017a].

Studies involving N→Sn intramolecularly coordinated organotin complexes have been significantly increased in the last decade. The introduction of organic substituent with N→Sn intramolecular coordination causes a change in the reactivity of organotin precursor leading to the isolation of various interesting structural motifs [Fard et al., 2009a, 2010]. Sn-O-Sn unit is the basic structural building block for organostannoxanes, and the stabilization of the Sn-O-Sn motif can be achieved either by using sterically bulky or chelating/intramolecular coordinating substituent on the Sn center of organotin precursor [Bouška et al., 2018; Chandrasekhar et al., 2013a]. N→Sn intramolecular coordination appears to be successful towards the isolation of molecular organotin assemblies with unsupported Sn-O-Sn motif. Padelcova *et al.* have reported a diorganotin chloride-oxide complex $[(L^{CN})_2SnCl]_2O$ (L^{CN}= 2-(N,N-dimethylaminomethyl)phenyl-) which contains a Sn-O-Sn bridge stabilized by four N→Sn intramolecular coordination [Padělková et al., 2013]. Recently, we have reported a dinuclear monoorganotin carboxylate $[(RSn)_2(\mu_2\text{-}O)(\mu_2\text{-}C_6H_5COO)_2(\eta\text{-}C_6H_5COO)_2]$ with Sn-O-Sn motif stabilized by N→Sn coordination [Mishra et al., 2021a].

Although the structural chemistry of organostannoxanes has been explored in great detail in the past, the presence of intramolecular coordination in the tin center provided another impetus to investigate this area further in terms of structure and applications. Dehnen *et al.* have successfully implemented the intramolecular O→Sn and N→Sn coordination approach on organotin sulfide assemblies resulting in a wide range of novel structures [Fard et al., 2009b;

Leusmann et al., 2015]. Jambor *et al.* have reported organotin sulfite and selenite involving N→Sn intramolecular coordination originating from N,C,N-chelating ligand {2,6-$(Me_2NCH_2)_2C_6H_3^-$} [Mairychová et al., 2011]. Jurkschat *et al.* have reported a series of crown ether substituted diorganotin halides involving O→Sn intramolecular coordination [Arens et al., 2013]. Ruzicka *et al.* have reported numerous organostannoxanes using N→Sn intramolecular coordination approach [Padělková et al., 2009]. Chart 9.1 depicts a few intramolecularly coordinated organostannoxanes reported in the literature [Bouška et al., 2009; Mishra et al., 2021b, 2021a].

On the other hand, the intermolecular interactions present in the coordination complexes have a major contribution to the field of supramolecular chemistry and crystal engineering. These interactions involve CH…N, CH…O, CH…S, CH…π, π…π stacking, etc., through different molecules present in the unit cell. Hirshfeld surface analysis is an important tool for analyzing the mode of packing, stability, and the interactive surfaces inside the crystal [Bomfim Filho et al., 2019; Soman et al., 2014; Tarahhomi et al., 2018; Yadav et al., 2016]. Although literature consists of numerous reports on fascinating supramolecular architectures shown by organostannoxanes, the surface studies of organostannoxanes are not much explored using Hirshfeld surface analysis.

Herein, in continuation of using N→Sn intramolecular coordination approach in organotin chemistry, we report the synthesis, structural characterization, and TD-DFT studies of a dinuclear diorganostannoxane $[(R_2Sn)_2(\mu_2\text{-}O)Cl_2]\cdot CH_2Cl_2$ (**9**), a mononuclear diorganotin complex $[R_2Sn(cupf)Cl]$ (**10**) and a dinuclear diorganotin carboxylate $[(R_2Sn)(\mu_2\text{-}OH)(OOCCH{=}CHC_6H_5)]_2\cdot 2H_2O$ (**11**) (R = 2-phenylazophenyl).

Chart 9.1 Representative examples of Organostannoxanes bearing N→Sn intramolecular coordination [Bouška et al., 2009; Mishra et al., 2021a, 2021b].

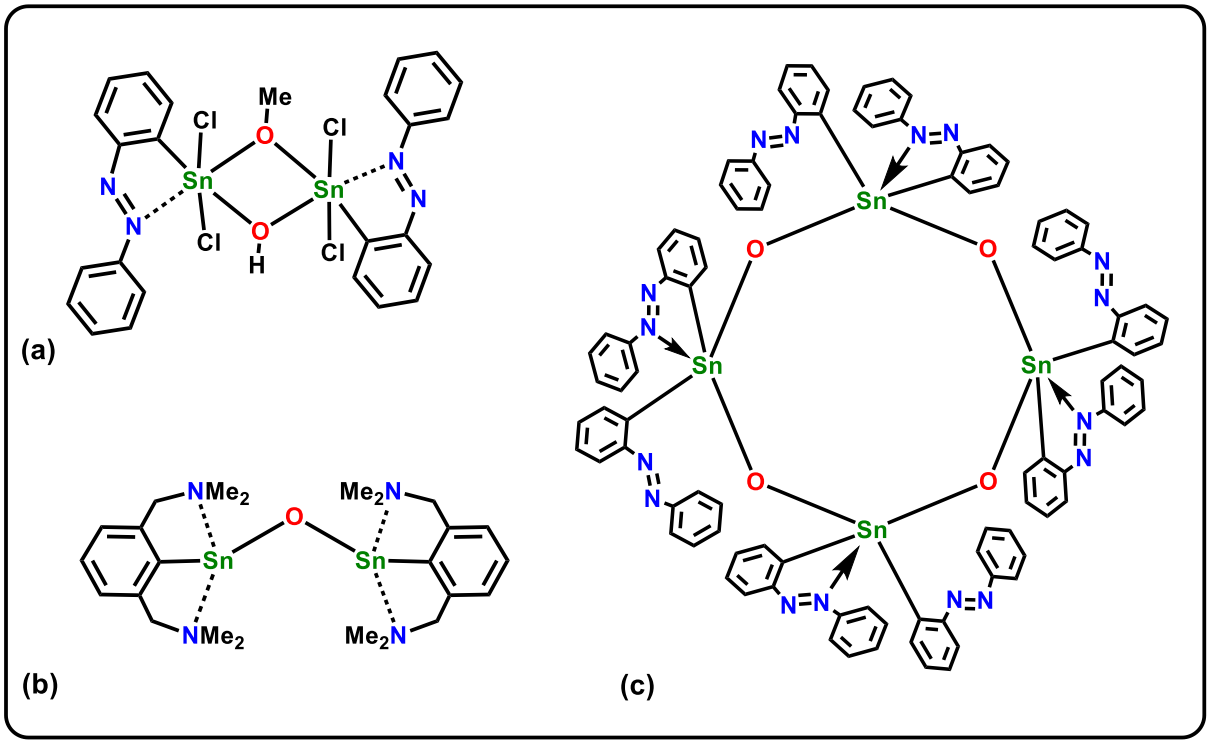

9.2 Experimental Section

9.2.1 Synthesis

[(R₂Sn)₂(μ-O)Cl₂]·CH₂Cl₂ (R = 2-phenylazophenyl) (9). NaOH (11 mg, 0.27 mmol) was added to a clear solution of R_2SnCl_2 (150 mg, 0.27 mmol) (R = 2-phenylazophenyl) in 20 ml of acetone/methanol (1:1) and the suspension was stirred at room temperature for 8 h. The clear yellow solution was filtered and kept for complete evaporation resulting into orange solid which was then dissolved in dichloromethane solvent. Yellow colored x-ray quality crystals

were collected after few days by the slow diffusion of hexane in dichloromethane solution. Yield (Based on R_2SnCl_2): 80 mg (56%). M.P. >230° C (decomp.); Elemental Analysis: Anal. Calcd for $C_{48}H_{36}Cl_2N_8OSn_2$: (1049.2) C, 54.95; H, 3.46; N, 10.68. Found C, 54.26; H, 3.56; N, 10.11. ^{1}H NMR (500MHz, $CDCl_3$, ppm): δ 8.4 (d), 7.8 (m), 7.5 (t), 7.2 (m), 7.1 (m). $^{13}C\{^1H\}$NMR (125MHz, $CDCl_3$, ppm): δ 135, 133, 132, 131, 130, 128, 122. ^{119}Sn NMR (186MHz, $CDCl_3$, ppm): δ -252.85; ESI-MS: $[(R_2Sn)Cl]^+$ 517; IR (KBr, cm^{-1}): 3426 (br), 3052 (w), 2922 (w), 2860 (w), 1606 (s), 1408 (m), 768 (m), 687 (m), 439 (w).

[R_2Sn(cupf)Cl] (R = 2-phenylazophenyl) (10). Cupferron (42 mg, 0.27 mmol) was added to a clear solution of R_2SnCl_2 (150 mg, 0.27 mmol) (R = 2-phenylazophenyl) in 20 ml of acetone/methanol (1:1) and the suspension was stirred at room temperature for 8 h. The clear dark yellow solution was filtered and kept for complete evaporation resulting into orange solid which was then dissolved in chloroform solvent. Yellow colored x-ray quality crystals were collected after few days by the slow evaporation of chloroform solution. Yield (Based on R_2SnCl_2): 130 mg (73%). M.P. >170° C (decomp.); Elemental Analysis: Anal. Calcd for $C_{30}H_{23}ClN_6O_2Sn$: (653.7) C, 55.12; H, 3.55; N, 12.86. Found C, 55.23; H, 3.57; N, 12.53. ^{1}H NMR (500MHz, $CDCl_3$, ppm): δ 8.4 (d), 7.9 (d), 7.8 (d), 7.7 (t), 7.6 (t), 7.4 (s), 7.0 (m). $^{13}C\{^1H\}$NMR (125MHz, $CDCl_3$, ppm): δ 151, 139, 134, 132, 131, 130, 129, 122, 119. ^{119}Sn NMR (186MHz, $CDCl_3$, ppm): δ -393; ESI-MS: $[R_2Sn(cupf)]^+$ 619.09. IR (KBr, cm^{-1}): 3468 (br), 3060 (w), 2924 (w), 2852 (w), 1470 (m), 1284 (s), 1212 (s), 911 (m), 761 (s), 682 (s), 423 (w).

[(R_2Sn)(μ_2-OH)($OOCCH=CHC_6H_5$)]$_2$ $2H_2O$ (R = 2-phenylazophenyl) (11). Cinnamic acid (45 mg, 0.3 mmol) and R_2SnO (150 mg, 0.3 mmol) (R = 2-phenylazophenyl) in 20 ml of dry toluene were heated to reflux for 6 h. Yellow clear solution was cooled to room temperature, filtered and kept for complete evaporation. The obtained yellow solid was dissolved in dichloromethane. X-ray quality crystals were obtained in two weeks by the slow diffusion of hexane in dichloromethane solution. Yield (Based on R_2SnO): 135 mg (70%). M.P. >220° C (decomp.); Elemental Analysis: Anal. Calcd for $C_{66}H_{52}N_8O_6Sn_2$: (1290.6) C, 61.42; H, 4.06; N, 8.68. Found C, 62.27; H, 4.37; N, 7.86. ^{1}H NMR (500MHz, $CDCl_3$, ppm): δ 8.1 (s), 7.7 (d), 7.5 (d), 7.3 (m), 7.1 (m), 6.5 (d). $^{13}C\{^1H\}$NMR (125MHz, $CDCl_3$, ppm): δ 135, 134, 132, 131, 129, 128, 122. ^{119}Sn NMR (186MHz, $CDCl_3$, ppm): δ -394; ESI-MS: [**3**+H^+] 1291.54; IR (KBr, cm^{-1}): 3434 (br), 3052 (w), 2922 (w), 1633 (s), 1366 (s), 1110 (m), 761 (s), 691 (m), 543 (w), 442 (w).

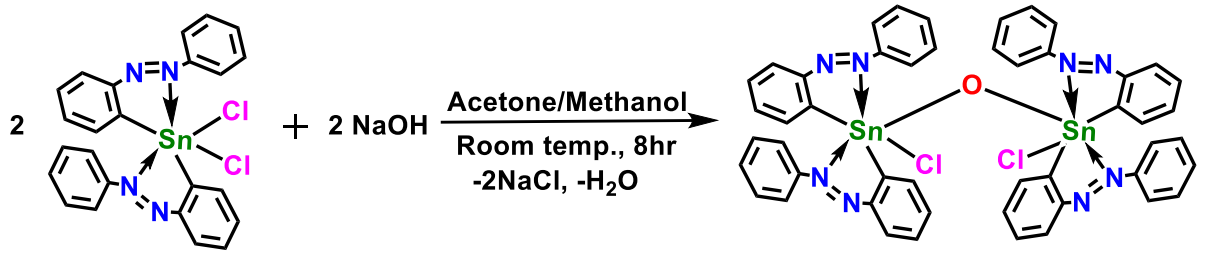

9

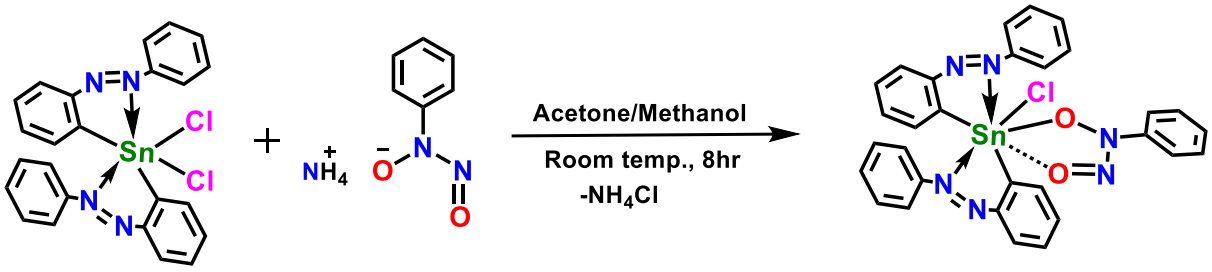

10

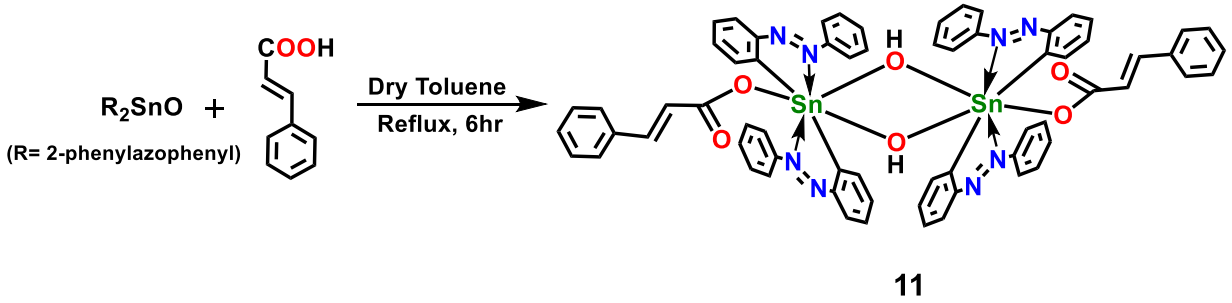

11

Scheme 9.1 Synthesis of complexes **9-11.**

9.2.2 Single-Crystal X-ray Crystallography

The details pertaining to the data collection and refinement for **9-11** are given in Table 9.1. As the solvent molecules were disordered with high thermal factor values in complexes **9** and **11** even at 100 K, squeeze analysis was performed using Program PLATON [Spek, 1999], and squeeze results were appended in the CIF file. The squeeze analysis shows that there are 168 electrons present per unit cell (Z=4) in **9,** which are assigned to one DCM solvent molecule, whereas 42 electrons per unit cell (Z=2) in **11,** which are assigned to two water molecules.

Table 9.1 Crystal data and structure refinement parameters for complexes **9-11.**

Identification code	**9**	**10**	**11**
Empirical formula	$C_{49}H_{38}Cl_4N_8OSn_2$	$C_{30}H_{23}ClN_6O_2Sn$	$C_{66}H_{56}N_8O_8Sn_2$
Formula weight	1134.12	653.68	1326.64
Temperature/K	100(2)	298(2)	100(2)
Crystal system	monoclinic	monoclinic	triclinic
Space group	$P2_1/c$	$P2_1/c$	P-1
a/Å	14.281(7)	11.961(11)	9.668(6)
b/Å	19.402(10)	12.790(12)	13.569(9)
c/Å	19.674(9)	19.206(17)	25.112(16)
α/°	90	90	76.115(9)
β/°	111.273(6)	93.295(11)	85.596(9)
γ/°	90	90	84.443(9)
Volume/Å^3	5080(4)	2933(5)	3178(4)
Z	4	4	2
ρ_{calc}g/cm^3	1.372	1.480	1.349
μ/mm^{-1}	1.129	1.000	0.841
F(000)	2088.0	1312.0	1304.0
Crystal size/mm^3	0.190 × 0.150 × 0.120	0.240 × 0.170 × 0.130	0.200 × 0.180 × 0.150
Radiation	MoKα (λ = 0.71073)	MoKα (λ = 0.71073)	MoKα (λ = 0.71073)
2Θ range for data collection/°	3.056 to 50	3.41 to 49.998	3.102 to 50.7
Index ranges	-16 ≤ h ≤ 16, 0 ≤ k ≤ 23, 0 ≤ l ≤ 23	-14 ≤ h ≤ 13, -15 ≤ k ≤ 15, -22 ≤ l ≤ 22	-11 ≤ h ≤ 11, -15 ≤ k ≤ 16, -30 ≤ l ≤ 30
Reflections collected	8928	32710	45869
Independent reflections	8928 [R_{int} = 0.0, R_{sigma} = 0.0491]	5172 [R_{int} = 0.0369, R_{sigma} = 0.0253]	11579 [R_{int} = 0.0735, R_{sigma} = 0.0698]
Data/restraints/parameters	8928/0/484	5172/0/380	11579/0/723
Goodness-of-fit on F^2	1.093	1.044	1.019

Final R indexes [I>=2σ (I)]	R_1 = 0.0483, wR_2 = 0.1247	R_1 = 0.0289, wR_2 = 0.0685	R_1 = 0.0547, wR_2 = 0.1225
Final R indexes [all data]	R_1 = 0.0680, wR_2 = 0.1335	R_1 = 0.0360, wR_2 = 0.0726	R_1 = 0.0954, wR_2 = 0.1441
Largest diff. peak/hole / e $Å^{-3}$	0.82/-0.51	0.61/-0.27	1.23/-0.42

9.2.3 Hirshfeld Surface Analyses

Hirshfeld surfaces, intermolecular interactions, and 2D fingerprint plots were generated for complexes **9-11** obtained from a single-crystal x-ray diffractometer using *Crystal Explorer 3.1* [Spackman et al., 2021]. d_{norm} surfaces were designed over a color scale of -0.200 to +1.000. d_{norm} is the normalized contact distance of a surface point to the nearest nucleus inside (d_i) and the surface point to nearest nucleus outside (d_e). 2D fingerprint plots were generated by using translated 0.8-3.0 Å range, including reciprocal contacts.

9.2.4 Theoretical Calculations

Density functional theory (DFT) calculations have been performed using Gaussian 09 [Frisch et al., 2009]. The geometrical optimizations were performed using the B3LYP functional and LanL2MB basis set for all atoms [Yanai et al., 2004]. The single point energy calculations and UV-vis absorption spectra were obtained with ORCA 4.0.1 software using time-dependent density functional theory (TD-DFT) [Neese, 2012]. TPSSH/def2-TZVPP basis set and RIJCOSX approximation with a tight SCF method have been used for TD-DFT calculations. The effect of solvent was taken into consideration using the conductor-like polarizable continuum model (CPCM) method with dichloromethane for complex **9** & **11** and chloroform for complex **10**.

9.3 Results and Discussion

9.3.1 Synthetic Aspects

The reaction of various organotin chlorides or oxides with numerous protic acids in different molar ratios/reaction conditions are known to generate diverse organostannoxanes. The dichloromethane (DCM) solvated **9** was synthesized by the partial hydrolysis of R_2SnCl_2 *(R = 2-phenylazophenyl)* using equimolar sodium hydroxide in the mixture of acetone/methanol (1:1) (Scheme 9.1) whereas complex **10** was synthesized by the equimolar room temperature reaction of R_2SnCl_2 and cupferron in the mixture of acetone/methanol (1:1) (Scheme 9.1). Complex **11** was the aqueous solvated dinuclear diorganostannoxane obtained by the reaction of R_2SnO and cinnamic acid in an equimolar ratio in refluxing dry toluene solvent (Scheme 9.1). ^{119}Sn NMR spectra of **9** and **11** showed a single resonance at δ -252 and -394 ppm, indicating the presence of chemically equivalent Sn centers, while that of complex **10** showed a signal at δ -393 ppm corresponding to the single Sn center(Fig. 9.1-9.3). Closer ^{119}Sn chemical shift values for complexes **10** and **11** can be attributed to the similar distorted heptacoordinated geometry around the Sn center. Similar intramolecular coordinated complex $[(L^{CN})_2SnCl]_2O$ (L^{CN}= 2-(N,N-dimethylaminomethyl)phenyl-) reported earlier indicated the ^{119}Sn NMR signal at -278 ppm, which is comparable to that of **9** [Padělková et al., 2013]. In the FTIR spectrum of **9-11**, vibrational bands at 439, 423, and 442 cm^{-1} correspond to the N-Sn interaction [Mishra et al., 2021d]. The ESI-MS spectrum of **9** and **10** revealed the absence of the parent ion peak, whereas it showed mass clusters centered at m/z = 517.02 for **9,** which is associated with the fragment $[(R_2Sn)Cl]^+$ while that of **10** peaks at m/z= 619.09 can be attributed to the fragment $[R_2Sn(cupf)]^+$. Complex **11** revealed the presence of parent ion peak $[(R_2Sn)(\mu_2\text{-}OH)(OOCCH{=}CHC_6H_5)]_2{+}H^+]$ centered at m/z = 1291.54. The absorption spectra of **9** and **11** were recorded in dichloromethane solvent (conc. 10^{-5} M), while that of **10** was recorded in chloroform solvent (conc. 10^{-5} M). Thermogravimetric analysis revealed the stability of the complex **9** and **11** to 290°C and 230°C, after which a sudden weight loss at 305°C and 260°C was observed, respectively, whereas, in the case of **10**, it showed two-step decompositions at 170°C and 280°C (Fig. 9.4-9.6).

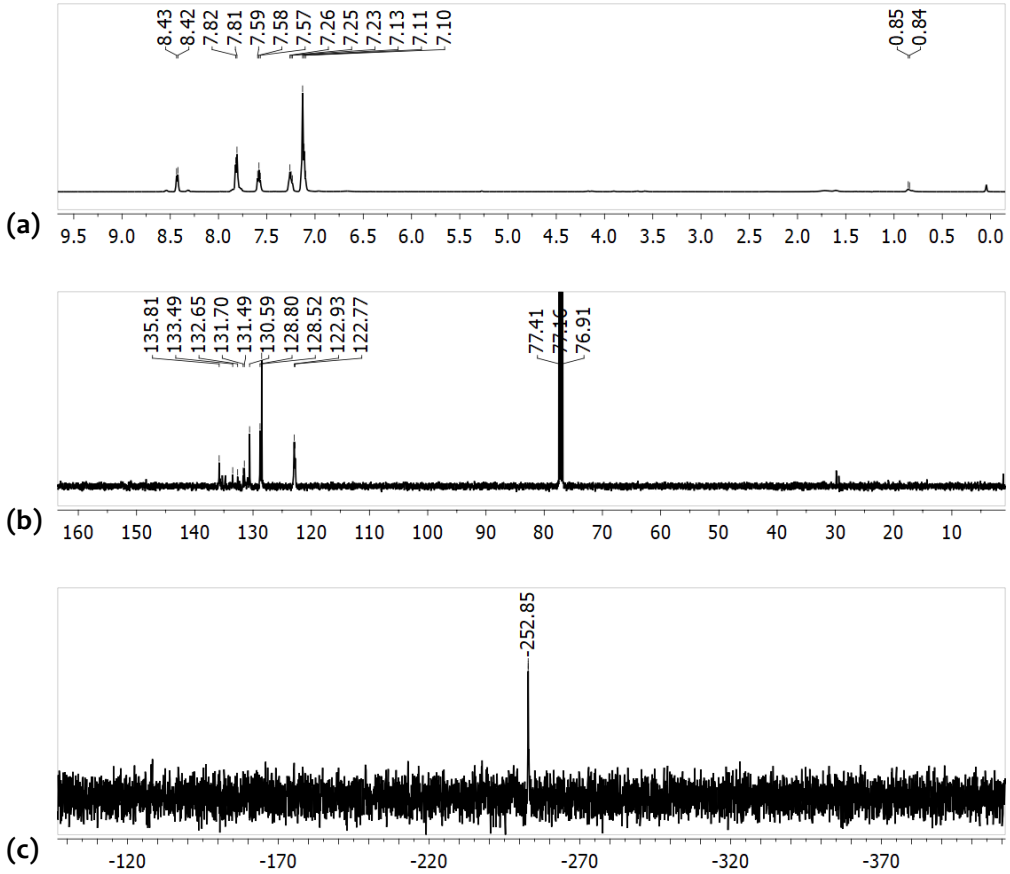

Fig. 9.1 (a) ^{1}H NMR, **(b)** ^{13}C NMR and **(c)** ^{119}Sn NMR of complex **9** recorded in $CDCl_3$.

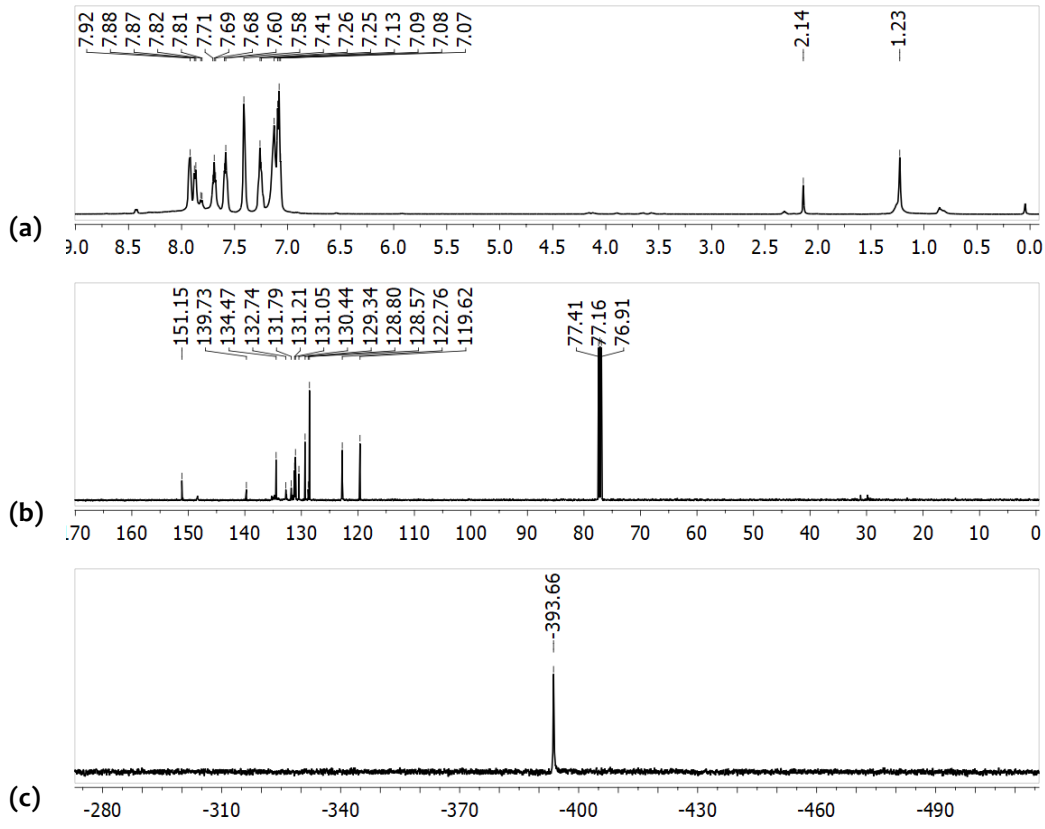

Fig. 9.2 (a) ^{1}H NMR, **(b)** ^{13}C NMR and **(c)** ^{119}Sn NMR of complex **10** recorded in $CDCl_3$.

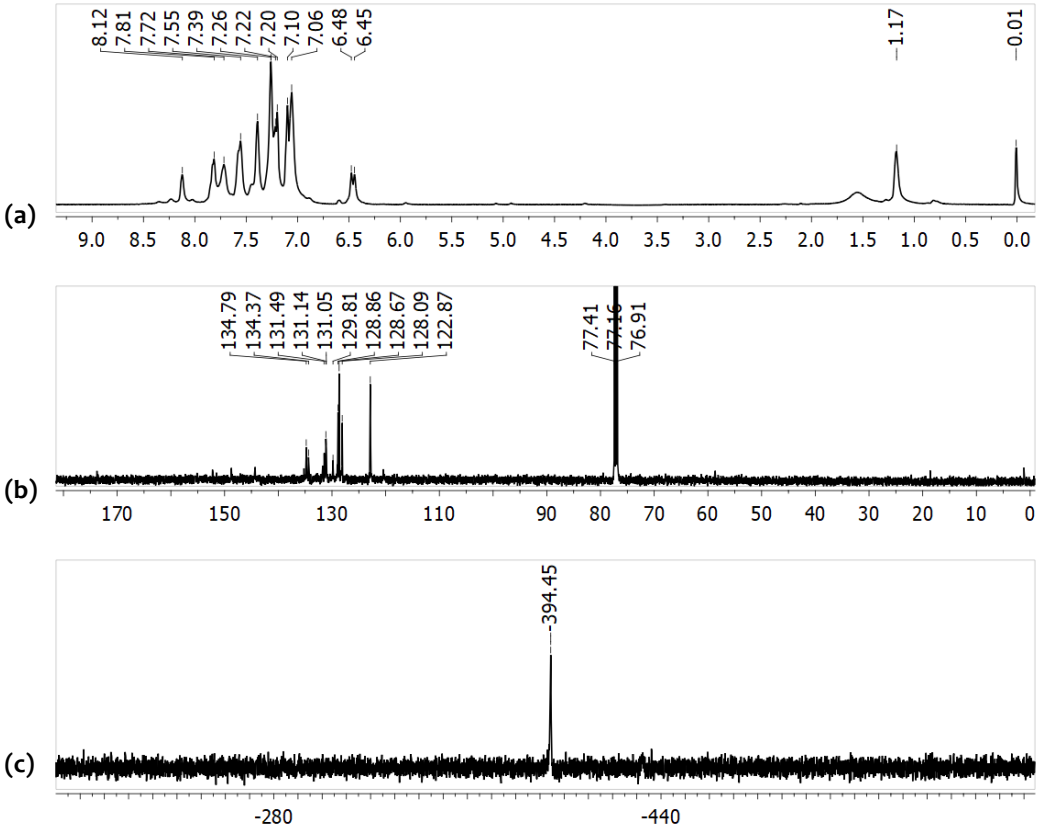

Fig. 9.3 (a) ^{1}H NMR, **(b)** ^{13}C NMR and **(c)** ^{119}Sn NMR of complex **11** recorded in $CDCl_3$.

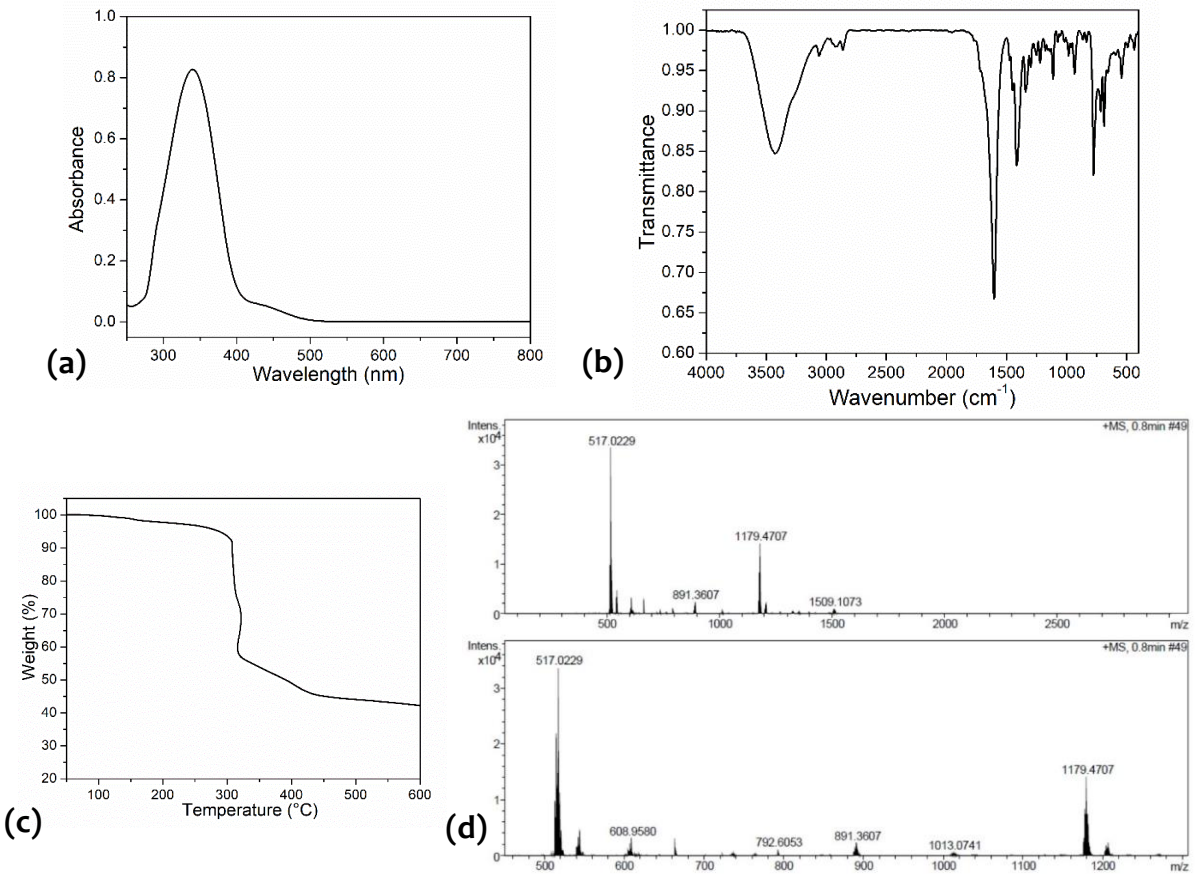

Fig. 9.4 (a) UV-Vis spectrum (conc. 10^{-5}M in DCM), **(b)** FTIR spectrum, **(b)** TGA (under N_2 atmosphere) and **(c)** ESI-MS spectrum of complex **9**.

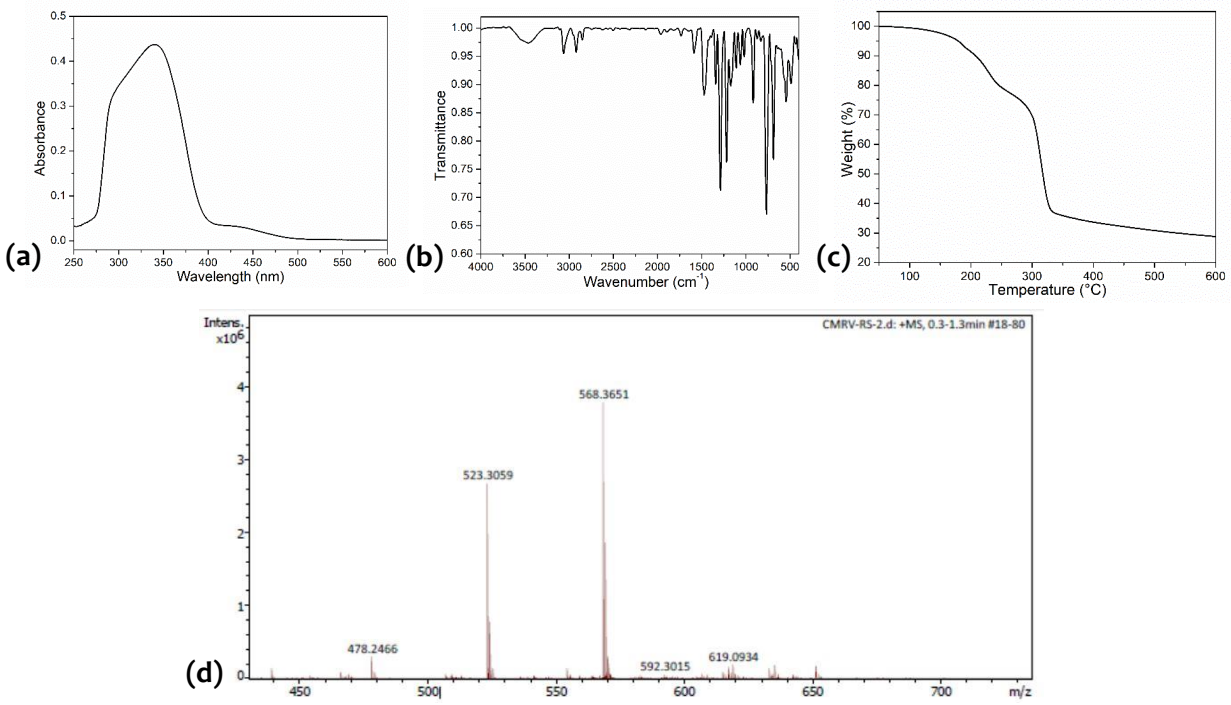

Fig. 9.5 (a) UV-Vis spectrum (conc. 10^{-5}M in DCM), **(b)** FTIR spectrum, **(b)** TGA (under N_2 atmosphere) and **(c)** ESI-MS spectrum of complex **10.**

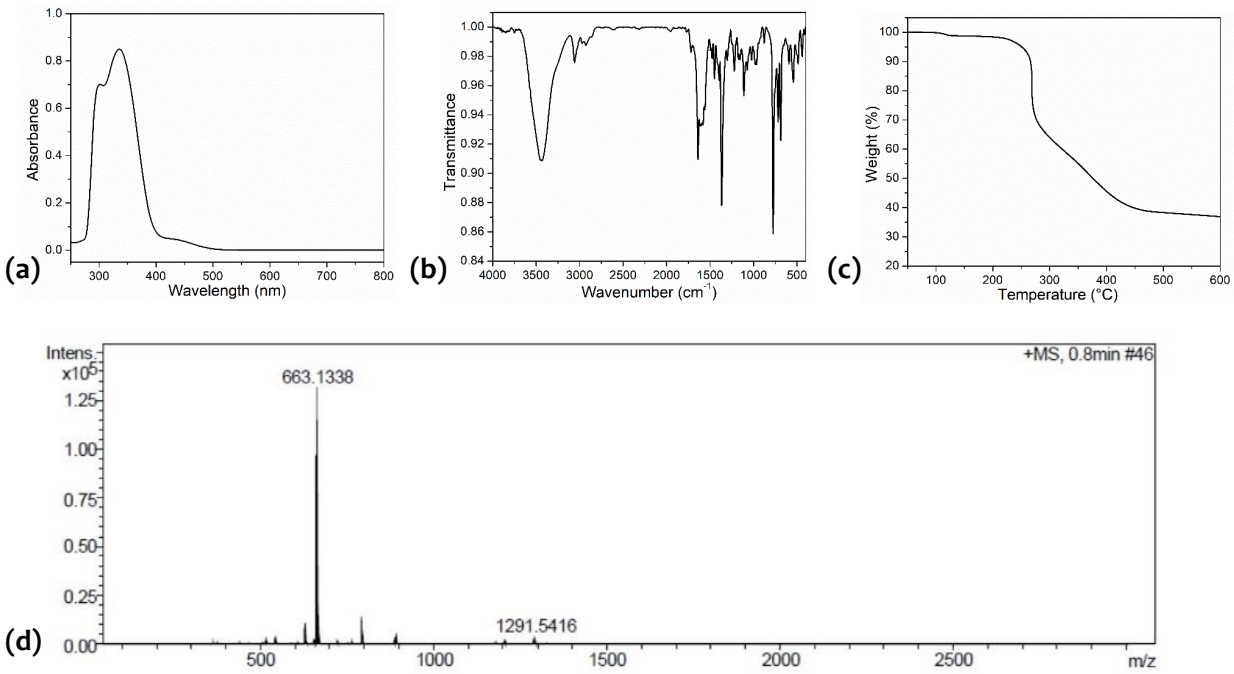

Fig. 9.6 (a) UV-Vis spectrum (conc. 10^{-5}M in DCM), **(b)** FTIR spectrum, **(b)** TGA (under N_2 atmosphere) and **(c)** ESI-MS spectrum of complex **11.**

9.3.2 Molecular and Supramolecular Structure of Complexes 9-11

Selected bond parameters of **9-11** are mentioned in the caption of Fig. 9.7-9.9. The molecular structure of **9** is shown in Fig. 9.7(a). Complex **9** consists of the simplest diorganostannoxane in which both the Sn centers (Sn1 and Sn2) are bridged through a μ_2-oxo ligand resulting in a rare unsupported Sn-O-Sn motif. The stabilization of the unsupported Sn-O-Sn motif is achieved by the intramolecular N→Sn coordination present in **9**. To the best of our knowledge, there is only one diorganostannoxane with a similar motif $[(L^{CN})_2SnCl]_2O$ (L^{CN}= 2-(N,N-dimethylaminomethyl)phenyl-) reported so far in the literature [Padělková et al., 2013].

Complex **9** retains both the N→Sn intramolecular coordination of the starting precursor R_2SnCl_2 (R = 2-phenylazophenyl) with the N→Sn bond distances, 2.61 and 2.71 Å, which are slightly larger than that of R_2SnCl_2, 2.51 and 2.58 Å [Briansó et al., 1983]. We have observed the hemi labile nature of N→Sn intramolecular coordination in $[R_2Sn(\mu\text{-}S)]_2$; (R = 2-phenylazophenyl) in our previous report. The Sn-O-Sn angle in the present instance is found to be 137.36°, whereas the Sn-S-Sn angle in $[R_2Sn(\mu\text{-}S)]_2$; (R = 2-phenylazophenyl) is 85.90° [Mishra et al., 2021c]. The smaller Sn-S-Sn angle in $R_2Sn(\mu\text{-}S)]_2$ suggests that steric factors appear to play a major role in the observed hemi labile nature of N→Sn coordination. The Sn-O bond distances of **9** are Sn1-O1, 1.9635(4)Å; Sn2-O1, 1.9617(4)Å and bond angles Sn1-O1-Sn2, 137.361(2)° are in close agreement with the literature precedent [Padělková et al., 2013]. Both the Sn centers of **9** are hexacoordinated [C1, C13, N2, N4, O1, and Cl1], possessing distorted octahedral geometry with the axial positions occupied by atoms Cl1 and N2, whereas equatorial ones are occupied by atoms C1, C13, N4 and O1 [Fig. 9.7(b)].

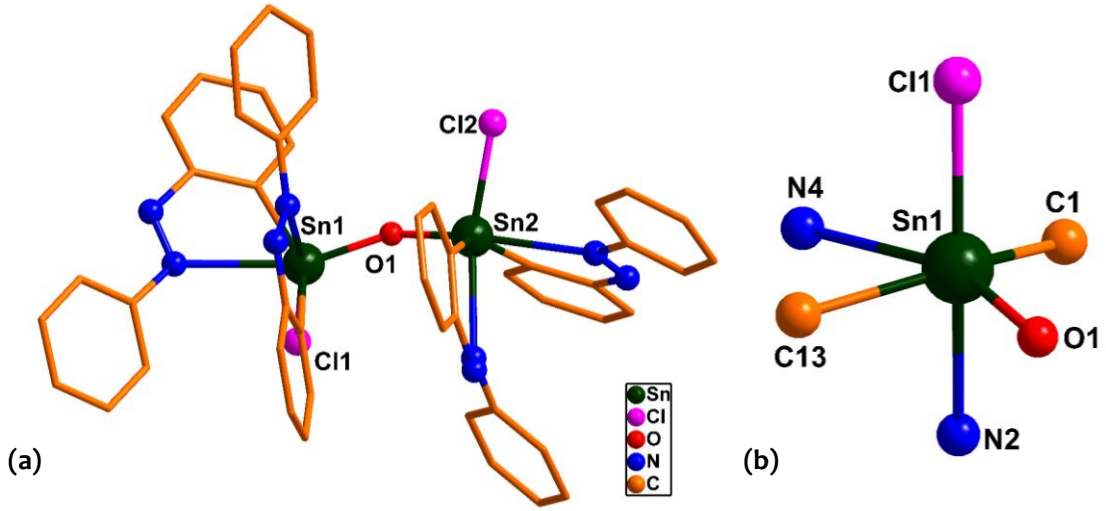

Fig. 9.7 (a) Molecular structure of complex **9**. Bond distance (Å) and bond angle (°) parameters: Sn1-O1, 1.9635(4); Sn2-O1, 1.9617(4); Sn2-Cl2, 2.4145(2); Sn1-O1-Sn2, 137.361(2)°; **(b)** coordination environment of Sn in complex **9**; Sn1-N2, 2.5223(5); Sn1-N4, 2.7509(4); Sn1-C1, 2.1423(4); Sn1-C13, 2.1310(5); Sn1-Cl1, 2.4229(2); Cl1-Sn1-N2, 162.92(1)°, N2-Sn1-N4, 74.699(1)°; Cl1-Sn1-C1, 96.37(1)°; N2-Sn1-O1, 95.022(1)°.

The molecular structure of **10** is shown in Fig. 9.8(a). Complex **10** is a substitution product of cupferron with R_2SnCl_2 achieved by substitution of one chloride by one cupferronato anion. There are no reports in the literature so far for cupferron coordinated diorganotin halide. The molecular structure of **10** reveals the bidentate coordination of the cupferronato ligand to the tin center resulting in a five-membered chelating ring. The five-membered SnO_2N_2 ring is almost planar, having a torsion angle (O1-N1-N2-O2) of -0.172 (4) Å. The chelating ring contains two different Sn-O bonds, i.e., Sn1-O1, 2.17(3) Å; Sn1-O2, 2.30(3) Å, and an N-N bond with bond distance N1-N2, 1.27(4) Å. The bond distances for coordinated cupferronato ligand O1-N1-N2-O2 (O1-N1, 1.328(3) Å; O2-N2, 1.261(4) Å; N1-N2, 1.270(4) Å) lie in the range between single and double bond which confirms the delocalization of π electrons. Cupferronato ligand makes an angle of 67.97 (9)° with Sn center (O1-Sn1-O2) in **10**. The formation of **10** retains both intramolecular N→Sn coordination with a little longer N→Sn bond distance (avg. 2.603Å) compared to the starting precursor, i.e., 2.55Å [Briansó et al., 1983]. The Sn center in **10** is heptacoordinated and possesses distorted pentagonal bipyramidal (PBP) geometry with atoms C7 and C19 of 2-phenylazophenyl at the axial position and 2O, 2N, and Cl [N4, N6, O1, O2, and Cl1] atoms at equatorial positions [Fig. 9.8(b)].

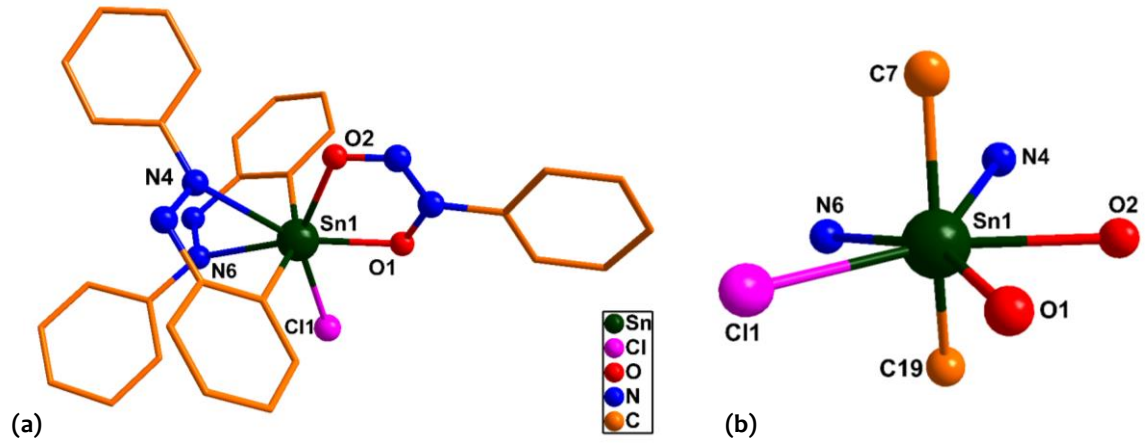

Fig. 9.8 (a) Molecular structure of complex **10**. Bond distance (Å) and bond angle (°) parameters: Sn1-O1, 2.1702(27); Sn1-O2, 2.3016(27); Sn1-Cl1, 2.4740(22); O1-Sn1-O2, 67.968(87)°; **(b)** Coordination environment of Sn in complex **10**; Sn1-N4, 2.6316(31); Sn1-N6, 2.5734(30); Sn1-C13, 2.1310(5); Sn1-C19, 2.1149(35); Sn1-C7, 2.1194(29); C19-Sn1-O2, 89.587(104)°, Cl1-Sn-O1, 747.770(68)°; Cl1-Sn1-C7, 95.042(77)°; N6-Sn1-N4, 68.277(80)°; N6-Sn1-C19, 70.192(108)°.

The molecular structure of **11** is shown in Fig. 9.9(a). Complex **11** consists of two crystallographically unique $[(R_2Sn)(\mu_2\text{-}OH)(OOCCH{=}CHC_6H_5)]$ units. Both the Sn center (Sn1 and Sn1') are connected through two μ_2-hydroxo ligands producing a cyclic four-membered Sn_2O_2 ring. All the four atoms of the ring lying on the same plane [Fig. 9.9(b)]. The Sn-O bond distances of the Sn_2O_2 ring (Sn1-O3, 2.0696(4) Å; Sn1-O3' , 2.1878(3) Å; Sn1' -O3, 2.1878(3) Å; Sn1' -O3' , 2.0696(4) Å) are in well agreement with the previous reports in the literature [Kundu et al., 2015a]. Each Sn center in **11** has a monodentate ($^-$OOCCH=CHC$_6$H$_5$) ligand unit. O2 atom of the carboxylate ligand is in close proximity to the hydroxy bridging and involved in the intramolecular hydrogen bonding [O2…H3, 1.843(4) Å] forming a six-membered cyclic ring on each side [Fig. 9.9(a)]. The formation of **11** retains both the intramolecular N→Sn coordination on each side with a slightly longer N→Sn bond distance compared to starting precursor. The Sn-O-Sn angle of the Sn_2O_2 ring in **11** is 111.16^o which is sufficiently wide (As discussed for **9**) to reduce the steric factor of 2-phenylazophenyl group resulting in the retention of both N→Sn intramolecular coordination. Each Sn center of **11** is heptacoordinated and possesses distorted PBP geometry with atoms C10 and C22 of 2-phenylazophenyl on axial position and 2N and 3O [N2, N4, O1, O3, and O3′] at equatorial positions [Fig. 9.9(c)].

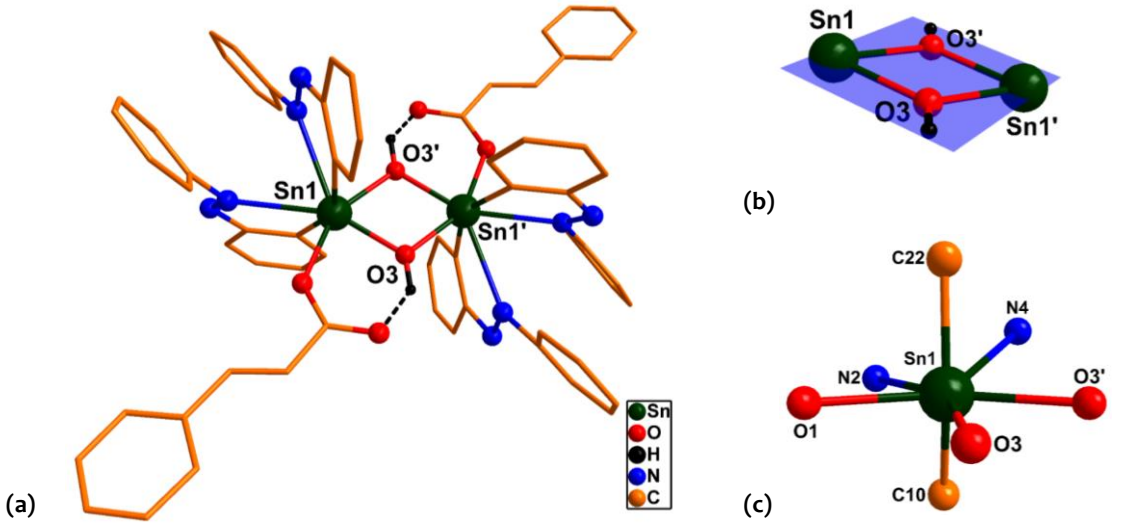

Fig. 9.9 (a) Molecular structure of complex **11**. Bond distance (Å) and bond angle (°) parameters: Sn1-O1, 1.9406(3); Sn1-O1', 1.9867(3); Sn1-O1-Sn1''', 129.396(1)°; O1-Sn1-O1', 104.482(1)°; H atoms are omitted for clarity. **(b)** Sn_4O_4 core structure with a plane passing through all atoms; **(c)** coordination environment of Sn in complex **11**; Sn1-C1, 2.1328(5); Sn1-C13, 2.1321(5); Sn1-N4, 2.6678(4); N4-Sn1-O1', 162.673(1)°, N4-Sn1-O1, 87.571(1)°; N4-Sn1-C1, 86.794(1)°; N4-Sn1-C13, 66.952 (1)°; C1-Sn1-C13, 129.258(2)°.

9.3.3 Hirshfeld Surface Analyses

To understand the surface phenomenon and the intermolecular interactions, molecular Hirshfeld surfaces and 2D fingerprint plots were generated using *Crystal Explorer 3.1* [Spackman et al., 2021]. Hirshfeld surfaces for complexes **9-11** mapped with normalized contact distance d_{norm} are shown in Fig. 9.10. In Fig. 9.10, the blue color shows that the sum of d_i and d_e is less than $d_{norm,}$ which indicates the longer contacts, whereas white and red indicate the Van der Waal separation and closer contacts, respectively. Fig. 9.10(a) displayed two intense red spots on the surface inside which Cl and H atoms are present, which are involved in the close contact with the atoms of the neighboring molecule through hydrogen bonding or CH…π interactions in the crystal packing. Similarly, in Fig. 9.10(b), two faded red spots indicate comparative weaker interactions with the neighboring molecules. In the case of complex **10**, Hirshfeld surfaces displayed three intense red spots on the surface, one arising due to oxygen of cupferranato ligand and the other two red spots arising due to H atoms of 2-phenylazophenyl and phenyl ring of the cupferronato ligand [Fig. 9.10(c) and (d)]. These atoms corresponding to three red spots are involved in the formation of supramolecular assemblies with neighboring molecules. Hirshfeld surfaces generated for complex **11** [Fig. 9.10(e) and (f)] showed intense red spots over the surface of the terminal oxygen atom of carboxylate ligand and H atoms of 2-phenylazophenyl group located far from the core depicting the possible intermolecular hydrogen bonding in the supramolecular assemblies.

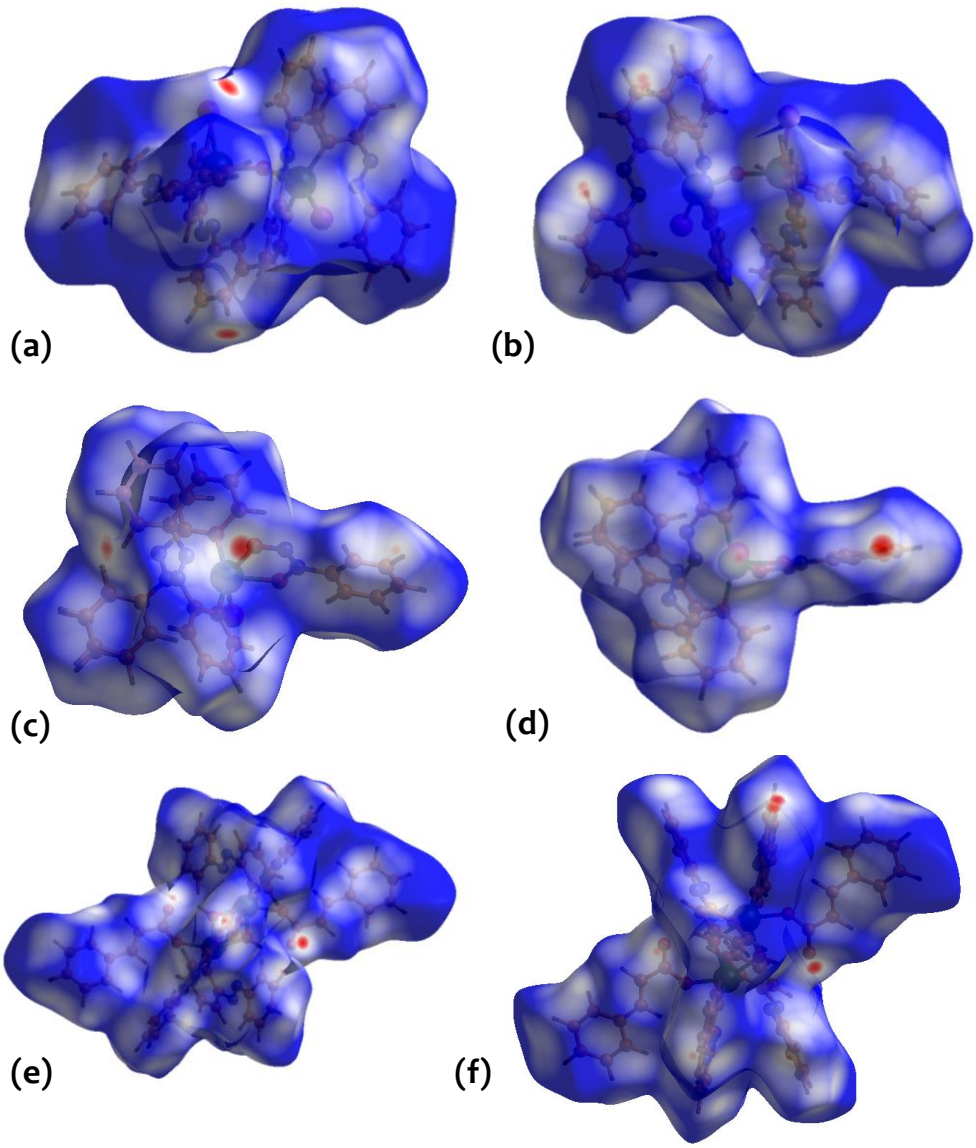

Fig. 9.10 Hirshfeld surfaces generated using d_{norm} over the color range of -0.200Å (red) to +1.000Å (blue) **(a), (b)** for complex **9**; **(c), (d)** for complex **10**; **(e), (f)** for complex **11.**

Packing inside the crystal is directly related to the presence of supramolecular interactions. 2D fingerprint plots of d_e vs. d_i for different types of interactions for complex **9-11** are illustrated in Fig. 9.11. 2D fingerprint plot for complex **9** displaying all the intermolecular interactions as well as individual interactions is shown in Fig. 9.11(a). Overall contributing interactions for complex **9** obtained from 2D plots are Cl…H, N…H, C…H, and non-directional H…H. The major contribution occurred from Cl…H/H…Cl (11%), C…H/H…C (20%), and N…H/H…N (5.5%) interactions which can be seen in Fig. 9.11(a). Whereas 2D plots for complex **10** revealed the major interactions contributing to the supramolecular assemblies are C…H/H…C (26.8%), Cl…H/H…Cl (6.7%), N…H/H…N (8.9%), O…H/H…O (3.3%) [Fig. 9.11(b)]. 2D plots for complex **11** are shown in Fig. 9.11(c), which depicts that the formation of supramolecular architectures is majorly accompanied by C…H/H…C (29.9%), N…H/H…N (6.2%), and O…H/H…O (3.8%) interactions. 2D fingerprint plots revealed the least contribution from C…C interaction which are 0.6%, 1.7% and 1.4% in complexes **9-11,** respectively. Some of the intermolecular interactions in the supramolecular assembly of complexes **9-11** are shown in Fig. 9.12. A closer Cl…H/H…Cl interactions were observed in the supramolecular assembly of complex **9** with a distance of 2.557 Å [Fig. 9.12(a)], whereas supramolecular assembly of complex **10** showed N…H/H…N (3.078 Å), O…H/H…O (2.329 Å), and Cl…H (2.960 Å) intermolecular interactions [Fig. 9.12(b)]. 1-D supramolecular chain of complex **11** revealed a closer O…H intermolecular interaction with a distance of 2.434 Å [Fig. 9.12(c)].

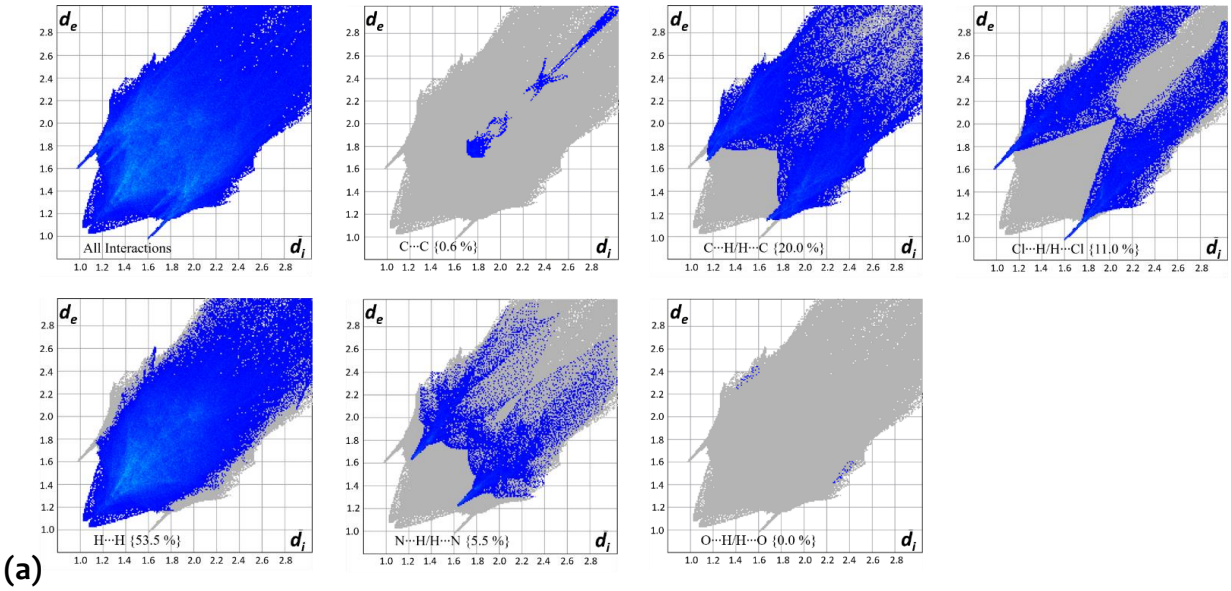

(a)

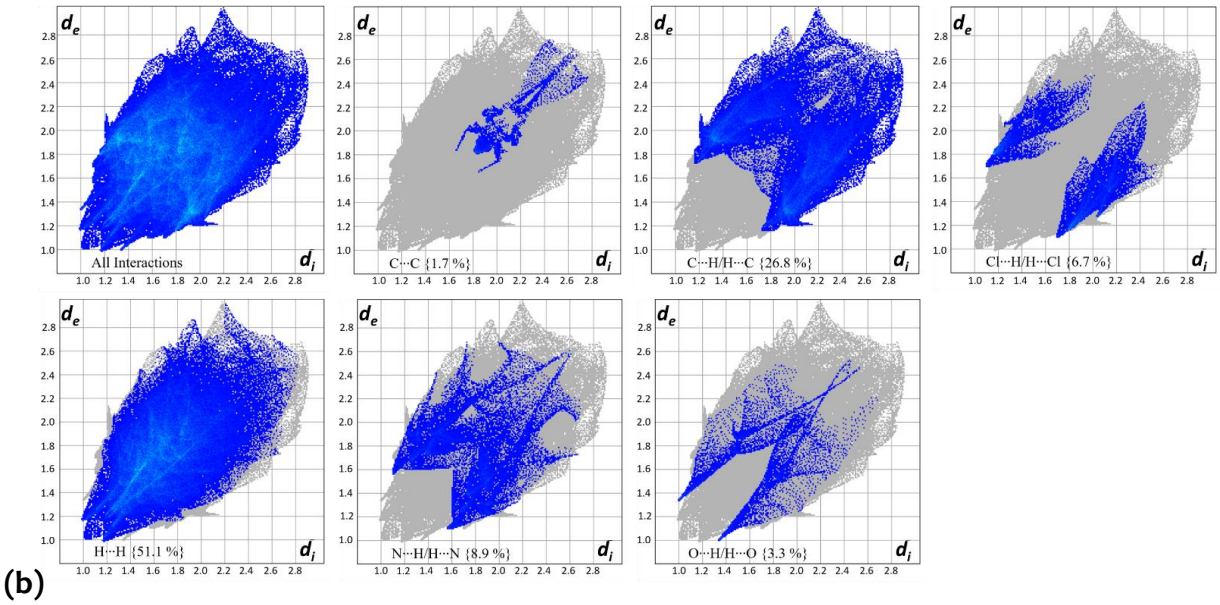

(b)

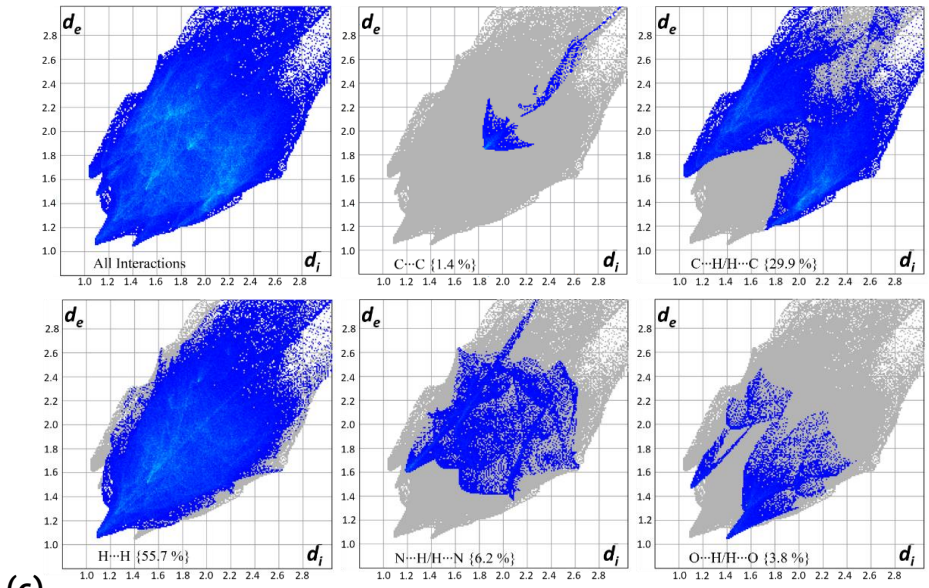

(c)

Fig. 9.11 2D fingerprint plots of d_e vs d_i ranging from 1.0 to 2.8 Å indicating different intermolecular interactions for **(a)** complex **9**, **(b)** complex **10**, **(c)** complex **11**.

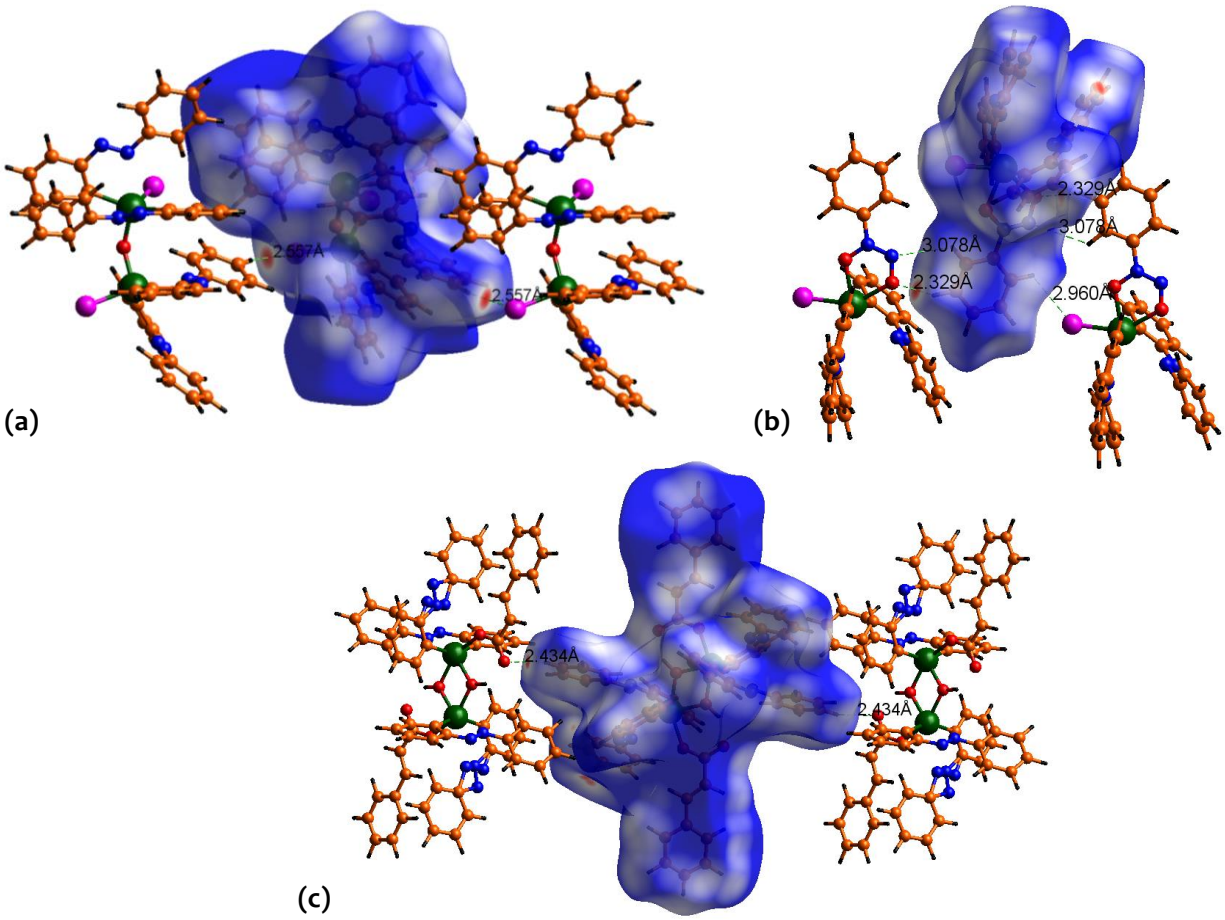

(a) (b) (c)

Fig. 9.12 Representation of some intermolecular interactions in the supramolecular assembly of **(a)** complex **9**, **(b)** complex **10**, and **(c)** complex **11**.

These intermolecular interactions were further studied with the help of *Diamond 3.1* software [Brandenburg et al., 2006] which turned out to be a well correlation with the interactions obtained from the 2D plots. 1-D and 2-D supramolecular architectures for complexes **9-11** are shown in Fig. 9.13-9.15.

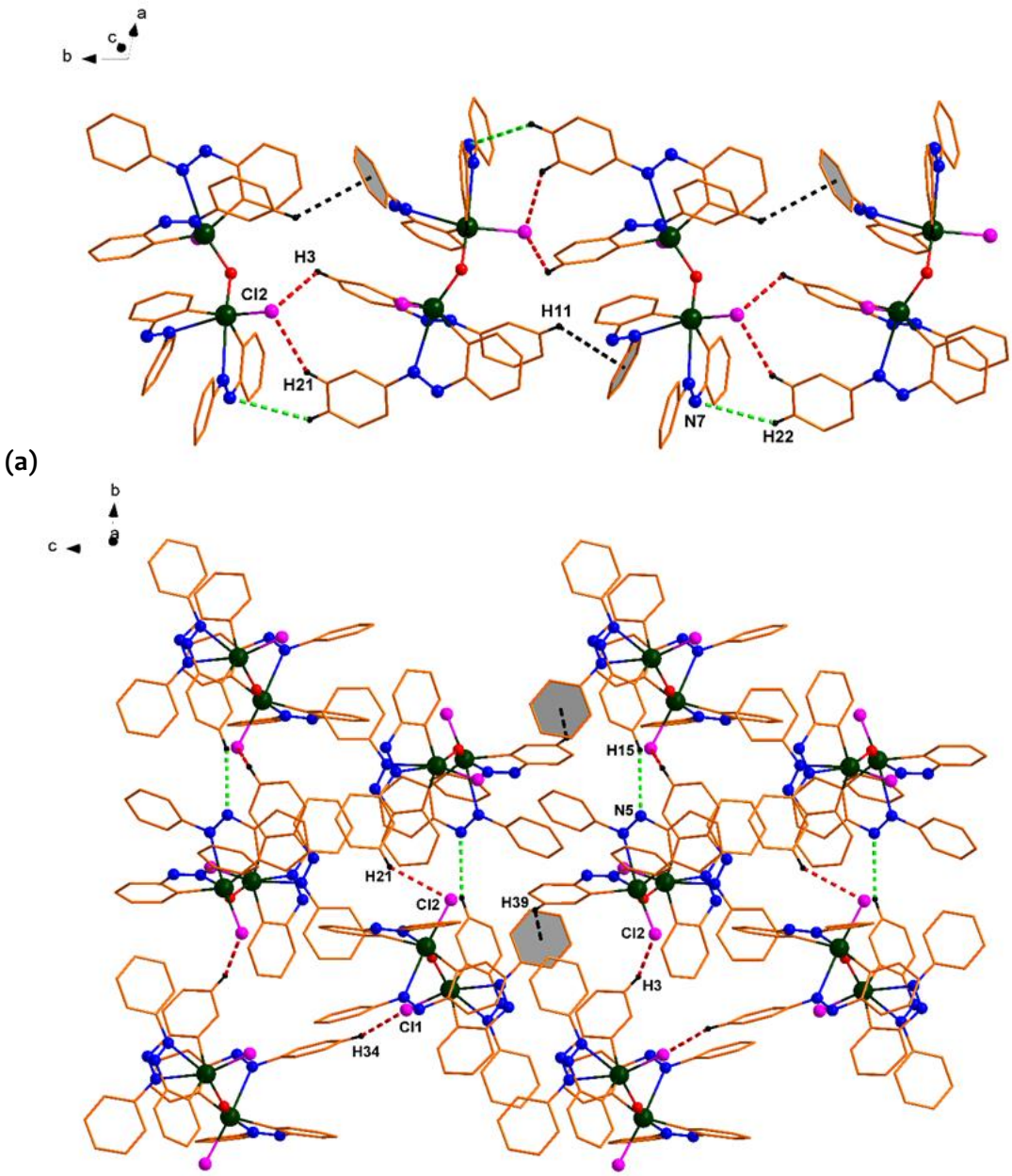

Fig. 9.13 (a) One-dimensional supramolecular assembly of **9** formed by C-H…π, N…H, and Cl…H interactions. Metric parameters are as follows; π-H11, 3.4963(1) Å; N7-H21, 3.3316(4) Å; Cl2-H3, 2.9810(2) Å; **(b)** Two-dimensional supramolecular architecture of **9** formed by CH…π, Cl…H interactions. H atoms are omitted to clarify the interactions. Metric parameters are as follows; π-H39, 3.0996(2) Å; Cl1-H10, 2.6799(2) Å; Cl2-H3, 2.9810(2) Å; Cl1-H34, 2.9021(2) Å; Cl2-H40, 3.5116(2) Å.

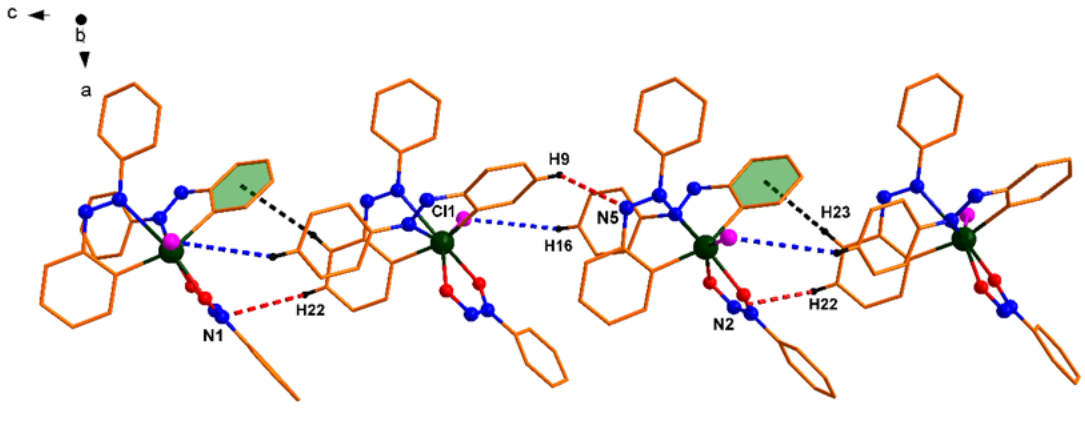

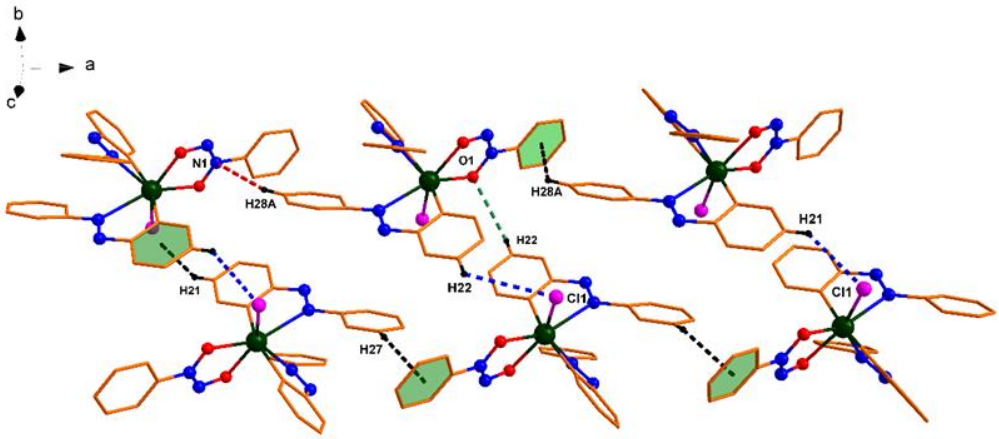

(b)

Fig. 9.14 (a) One-dimensional supramolecular assembly of **10** formed by C-H…π, N…H, and Cl…H interactions. Metric parameters are as follows; π-H23, 3.3706(19) Å; N1-H22, 3.36368(35) Å; Cl1-H16, 3.6916(33) Å; N2-H22, 3.4101(38) Å; **(b)** Two-dimensional supramolecular architecture of **10** formed by CH…π, O…H, N…H, Cl…H interactions. H atoms are omitted to clarify the interactions. Metric parameters are as follows; π-H21, 3.9157(27) Å; π-H27, 2.9692(19) Å; π-H28, 3.9028(33) Å; Cl1-H22, 3.7584(32) Å; Cl1-H21, 3.0405(19) Å; N1-H28A, 3.1813(32) Å; O1-H22, 3.2306(33) Å.

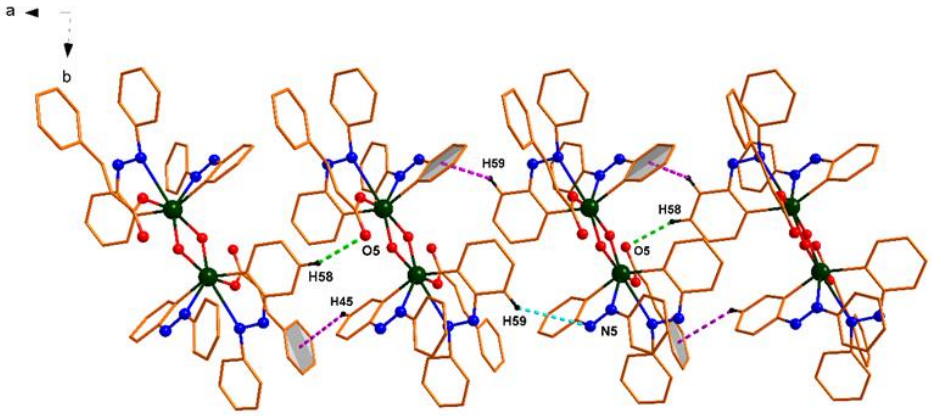

(a)

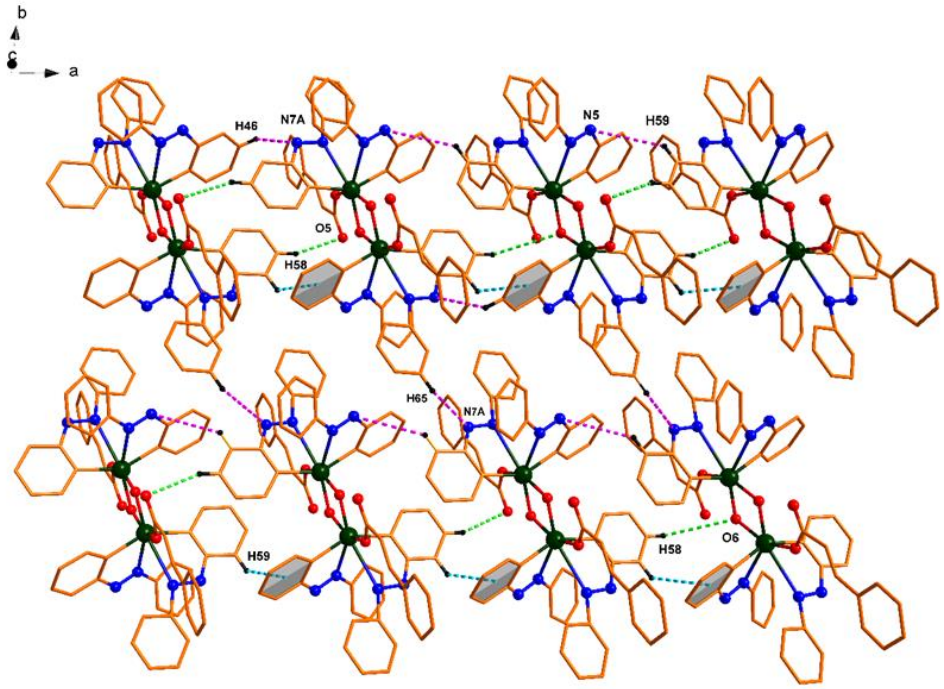

(b)

Fig. 9.15 (a) One-dimensional supramolecular assembly of **11** formed by C-H…π, N…H, and O…H interactions. Metric parameters are as follows; π-H45, 3.6709(15) Å; π-H59, 3.7268(18) Å; N5-H59, 3.5298(61) Å; O5-H58, 2.6753(46) Å; **(b)** Two-dimensional supramolecular architecture of **11** formed by π-H, N…H, O…H, interactions. H atoms are omitted to clarify the interactions. Metric parameters are as follows; π-H59, 3.7268(18) Å; N7A-H65, 3.6292(131) Å; N7A-H46, 3.626 Å; O6-H58, 3.5987Å.

9.3.4 Photophysical Studies

TD-DFT studies were performed in collaboration. To understand the photophysical properties of the complexes, we have calculated the highest occupied molecular orbital (HOMO) and lowest unoccupied molecular orbital (LUMO) using DFT. The HOMO for the three complexes were found at -6.86 eV, -6.41 eV and -3.29 eV, while LUMO at -3.52 eV, -3.0 eV and -0.34 eV respectively. The calculated HOMO-LUMO gaps are 3.34 eV, 3.41 eV, and 2.95 eV. The HOMO of complex **9** consists of π orbitals of two 2-phenylazophenyl substituents, and as expected, the LUMO has the contribution of π* orbitals of the same ligands [Fig. 9.16(a)]. The HOMO of complex **10** is due to the nonbonding p-orbitals of oxygen and chlorine atoms, while LUMO consists of π* orbitals of 2-phenylazophenyl substituent [Fig. 9.16(b)]. For complex **11**, the HOMO is contributed by p orbitals of oxygen atoms, and LUMO is contributed by antibonding π* orbitals of 2-phenylazophenyl substituent [Fig. 9.16(c)].

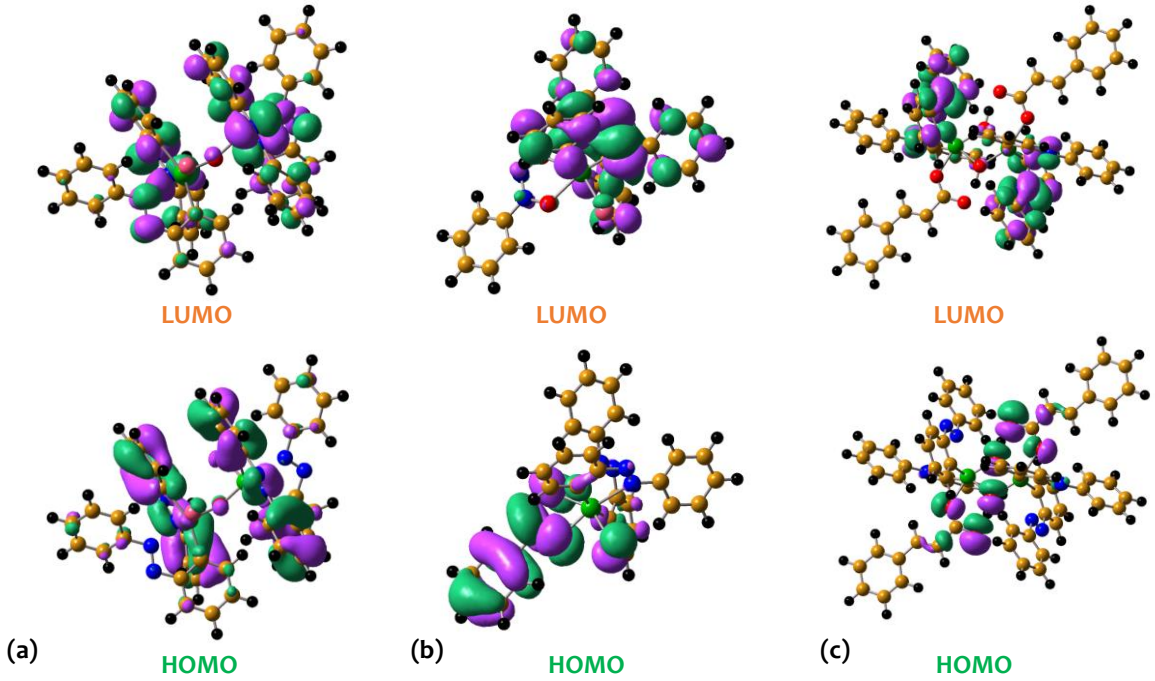

Fig. 9.16 (a)-(c) Calculated Highest Occupied Molecular Orbitals (HOMO) and Lowest Unoccupied Molecular Orbitals (LUMO) using density functional theory for complexes **9, 10,** and **11,** respectively.

Complex **9** shows one broad absorption band at 339 nm experimentally, which matches our theoretically calculated absorption spectrum [Fig. 9.17]. Using TD-DFT, the prominent band

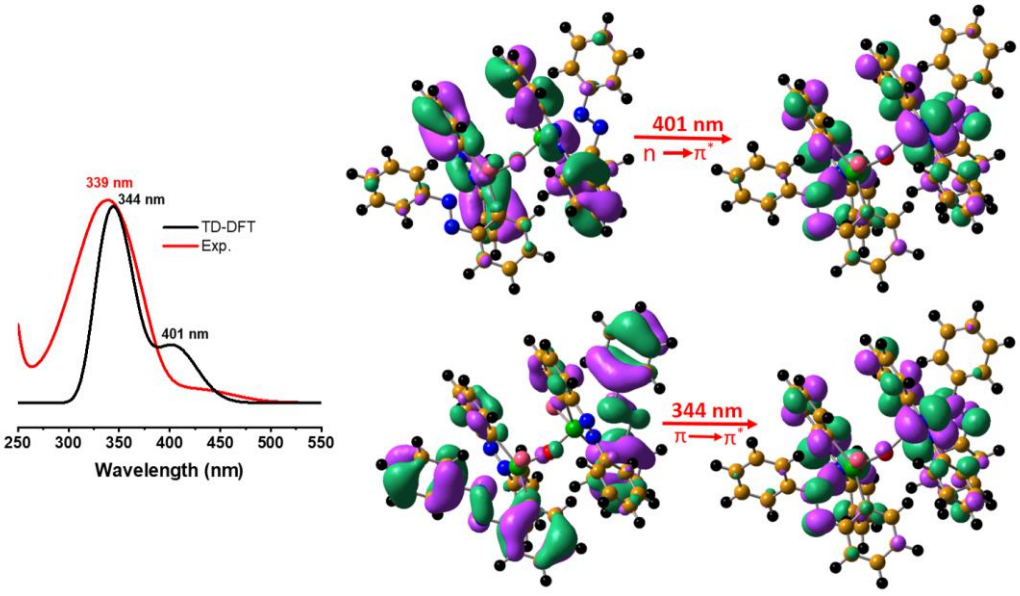

Fig. 9.17 Comparative study of UV-vis absorption spectra and corresponding orbital transition of complex **9.** The black line shows theoretical analysis, and the red line shows experimental absorption spectra.

with high extinction coefficient occurs at 344 nm, and another band appears at 401 nm with lower absorption. The prominent band arises due to π orbitals of the 2-phenylazophenyl ligand to the corresponding π* orbital transition. Another band at a higher wavelength of 401 nm is due to the nonbonding n orbital of the tin and oxygen atom to antibonding π* orbital transition.

The experimental UV-vis spectrum of complex **10** shows one broad absorption band at 340 nm [Fig. 9.18]. TD-DFT calculation suggested one intense band at 354 nm with a high extinction coefficient, identical to experimental data. As expected, the band is arising due to nonbonding n orbital of chlorine and oxygen atoms and π orbital of ligands to π* orbital transition. The other two bands with lower extinction coefficients arose at 420 nm and 318 nm, but these bands could not be resolved because of the broadness of the experimental spectrum. The corresponding transitions are n to π* and n+ π to σ* for 420 nm and 318 nm peaks.

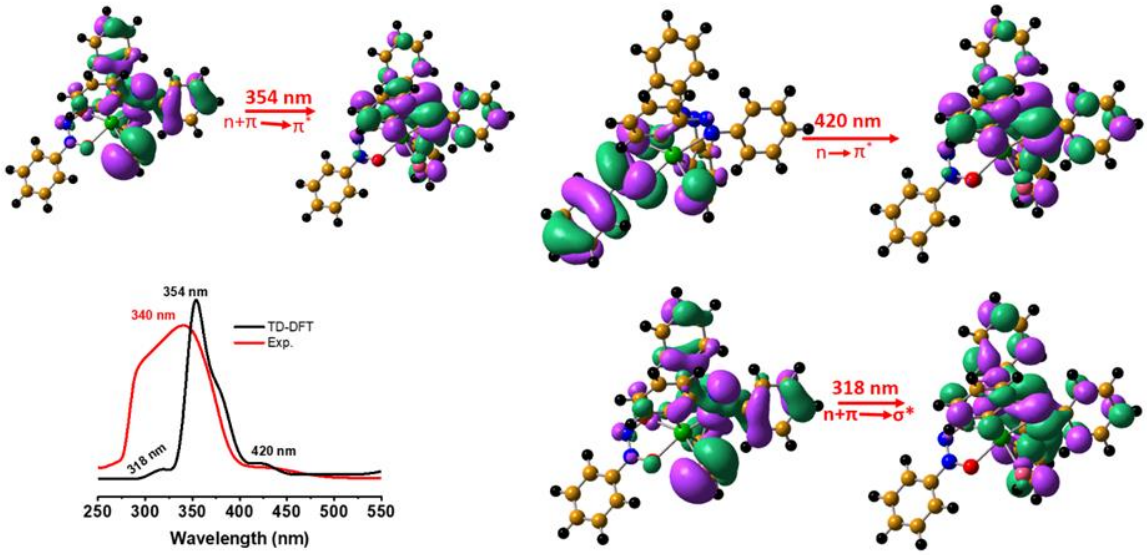

Fig. 9.18 Comparative study of UV-vis absorption spectra and corresponding orbital transition of complex **10**. The black line shows theoretical analysis, and the red line shows experimental absorption spectra.

Complex **11** shows two experimental absorption bands, one prominent band at 336 nm and another band with a comparatively lower extinction coefficient at 305 nm. Theoretical calculations also predict a similar absorption band at 345 nm and 318 nm, respectively [Fig. 9.19]. Another band also arises at 398 nm, which is not resolved experimentally. The prominent absorption band occurs due to the transition between π orbital of the azo group to π* orbital of 2-phenylazophenyl substituent. The band at 398 nm is arising between the HOMO to LUMO transition of the molecule. Another transition occurs from nonbonding p orbital of oxygen to antibonding π* and σ* orbital of 2-phenylazophenyl substituent at 318 nm.

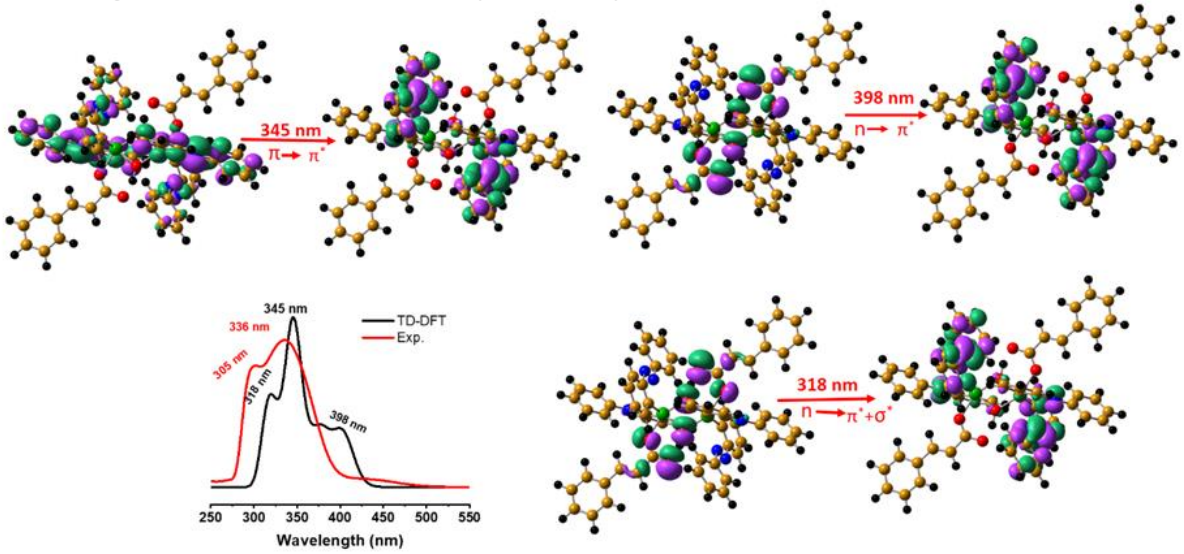

Fig. 9.19 Comparative study of UV-vis absorption spectra and corresponding orbital transition of complex **11**. The black line shows theoretical analysis, and the red line shows experimental absorption spectra.

9.4 Conclusion

Three molecular diorganotin complexes (**9-11**) containing Sn-O units are synthesized using an intramolecular coordination approach. Complex **9** is a dinuclear diorganostannoxane with a rare unsupported Sn-O-Sn motif $[(R_2Sn)_2(\mu_2\text{-}O)Cl_2]\cdot CH_2Cl_2$ **(9).** The other two complexes are a mononuclear diorganotincupferronato complex $[R_2Sn(cupf)Cl]$ **(10)** and a dinuclear diorganotin carboxylate $[(R_2Sn)(\mu_2\text{-}OH)(OOCCH{=}CHC_6H_5)]_2\cdot 2H_2O$ **(11)** (R= 2-phenylazophenyl). The molecular structure of the complexes **9-11** was primarily established with single-crystal x-ray crystallography and further supported with FTIR, UV, ESI-MS, ^{1}H, ^{13}C, and ^{119}Sn NMR spectroscopy techniques. TD-DFT calculations revealed that π→π* and n→π* are the prominent ligand-to-ligand transitions occurring in these complexes. Hirshfeld surfaces were mapped with normalized contact distance d_{norm}, which revealed the interactive surface sites with the help of d_i, d_e distances of the complexes **9-11**. 2D fingerprint plots revealed the majorly contributing intermolecular interactions present in the crystal packing, i.e., C…H/H…C, Cl…H/H…Cl, N…H/H…N and O…H/H…O interactions.

…